Helicon wave plasma generated by a resonant birdcage antenna: magnetic field measurements and analysis in the RAID linear device

Ph Guittienne, R Jacquier, B Pouradier Duteil, A A Howling[*] ,
R Agnello and I Furno

Ecole Polytechnique Fédérale de Lausanne (EPFL), Swiss Plasma Center (SPC), CH-1015 Lausanne, Switzerland

E-mail: alan.howling@epfl.ch

Abstract

This paper describes a helicon-wave-sustained plasma generated by a novel birdcage antenna with cosine azimuthal current distribution. The resonant birdcage source maintains a stable intense plasma column from low (300 W) to high (10 kW) steady-state RF power in hydrogen or argon, enabling plasma diagnostic measurements over the whole volume. The plasma density, 10^{18} to 10^{19} m^{-3}, and uniform static magnetic field, 200–800 G, are typical of high density, low B-field helicon sources where the RF excitation frequency, 13.56 MHz here, is far above the ion cyclotron frequency and much lower than the electron cyclotron and plasma frequencies. Magnetic field measurements of the unbounded plasma column show a helicon wave propagating from the birdcage source to the target 1.5 m away. The axial wavelength, measured for a range of plasma density and magnetic field, is described by the whistler dispersion relation; it is not determined by the antenna length but varies smoothly as a function of electron density irrespective of the gas type, and shows no discontinuous transitions. This wavelength was compared with semi-analytical and purely numerical models, showing a good fit with the $m = +1$ helicon eigenvalue of shortest axial wavelength. The birdcage resonant antenna is a suitable source for continuous helicon-sustained plasma experiments, from fundamental wave studies up to high power applications in hydrogen or deuterium.

Keywords: resonant birdcage antenna, helicon plasma, magnetic field, hydrogen plasma

(Some figures may appear in colour only in the online journal)

1. Introduction

In the framework of plasma physics, whistler waves are electromagnetic modes that can propagate in magnetized plasma at frequencies much lower than the electron plasma frequency which is the low frequency limit for wave propagation in non-magnetized plasma [1–8]. In nature, whistler waves can notably be detected in the ionosphere/magnetosphere where they are triggered by lightning, at frequencies typically in the kHz range. In the context of plasma sources, it was shown by Boswell in the early 1970s [9–11] that the excitation of whistler waves in magnetized plasma by means of suitably-shaped RF antennas can generate high electron density in plasma extending far away from the source along the magnetic field. These sources are often partial-helix antennas, popularized as 'helicon sources', where the term helicon conventionally designates bounded whistler modes of cylindrical symmetry.

---

[*] Author to whom any correspondence should be addressed.

Preliminary evidence of helicon wave generation by an alternative antenna, the cylindrical resonant network (birdcage), was given in 2005 [12]. More recently, the resonant antenna ion device (RAID) experiment was developed [13–17] where a resonant birdcage antenna is used as a helicon plasma source [18, 19] in the initial step to investigate negative ion production for neutral beam heating of tokamaks. Powerful helicon sources of hydrogen and deuterium ions, currently with 10 kW long-pulse operation [20], are also projected for fusion-relevant plasma material interaction experiments up to 200 kW [21–24].

The RAID experiment is also well suited for fundamental studies of helicon wave propagation. A radially-unbounded, steady-state plasma column, typically 1.5 m long, is maintained in the main vacuum chamber where it can be conveniently measured, axially and radially, by various diagnostics. The discharges were thoroughly characterized in terms of electron density mappings [16, 17], which are necessary for the analysis of the helicon wave dispersion relation. The helicon wave field was then investigated by means of a three-dimensional magnetic field (*B*-dot) probe [15]. The results presented here show the first formal proof of helicon wave generation by resonant network antennas.

In addition to the observation of a wave field structure consistent with helicons, the axial wavelength was measured for a range of plasma density and external magnetic field strength. These experimental results are compared with both semi-analytical and purely numerical models, showing a good fit with the $m = +1$ helicon eigenvalue of shortest axial wavelength.

This paper is structured as follows: section 2 presents the RAID linear device with emphasis on the birdcage antenna. The experimental demonstration of helicon waves is given in section 3. Helicon mode theory is developed analytically and by numerical simulation in section 4 for comparison with the measurements. The conclusions are presented in section 5.

2. Experimental setup: the RAID linear device, resonant birdcage antenna, and diagnostics

RAID, shown schematically in figure 1, is a linear and axisymmetric plasma reactor [13]. The resonant birdcage plasma source, on one end, is principally inductively coupled to the plasma by high currents oscillating in the legs at the RF excitation frequency of 13.56 MHz. The birdcage antenna is described in section 2.1.

The helicon wave propagates along the static magnetic field $\mathbf{B}_0$ produced by 5 Helmholtz coils around the cylindrical chamber. The leftmost coil in figure 1 can be used to produce a counter-field at the birdcage source, but was not used in these experiments. Therefore, apart from the diverging magnetic field at the ends of the coils where the source is situated, the magnetic field $\mathbf{B}_0$ was approximately uniform over the plasma column region of probe measurements (0–134 cm) as shown in figure 1. The plasma, whether in argon or in hydrogen, is an intensely bright narrow column [11, 25], approximately 5 cm diameter, which is effectively unbounded

radially within the much wider RAID vacuum chamber of 40 cm diameter [3, 4]. The plasma within this chamber is 134 cm long, bounded by a 12 cm diameter water-cooled copper block with a molybdenum surface target which protrudes 14 cm into the chamber as shown in figure 1, to protect the rear vacuum chamber wall from excessive heat load. The birdcage antenna, in air, is mounted around a double-walled, high-thermal-conductivity alumina cylinder with 8 water-cooling channels, permitting continuous operation up to 10 kW RF power [13, 20]. The double cylinder, external diameter 11.5 cm, internal diameter 9.5 cm and 38 cm long, is protected internally on the back side by dielectric foam to withstand the heat flux. Experiments in this paper were performed by injecting Ar and H_2 gases, typically at 3 and 10 sccm respectively, into the vacuum chamber at a pressure between 0.1 and 1 Pa, with static magnetic field 130–850 G, and RF continuous power 800–5000 W.

2.1. Resonant birdcage antenna

The birdcage is a novel source [13] for helicon-wave-sustained plasma which is fundamentally different from the conventional partial helix antennas, so its design will be described here in detail. The 13 cm diameter birdcage antenna shown in figure 2(a) is a resonant, high-pass network [12, 26] consisting of $N = 9$ identical parallel leg inductances joined by 16 identical capacitor assemblies. The leg inductances are straight copper tubes, $l = 15$ cm long and $a = 0.3$ cm radius with effective self partial inductance [27] $L \approx \frac{\mu_0}{2\pi} l \left(\ln \left[\frac{2l}{a} \right] - 1 \right) = 0.108$ μH, cooled by internal water flow. Each capacitor $C = 4$ nF $\pm 2\%$ is a parallel assembly of 10 low loss ceramic capacitors. The legs are soldered to brass segments which hold the screwed capacitor assembly plates. The birdcage is mounted around the alumina cylinder and is surrounded by two, half-cylinder, electrically-floating aluminium screens (see the inset of figure 11) whose radial position can be adjusted for fine tuning, ± 0.6 MHz, of the resonance frequency. The whole assembly is mounted inside a metal box Faraday cage which forms the ground reference for the birdcage and the screen of the RF power input coaxial cable. The overall diameter and length of the birdcage antenna are similar to partial helix antennas used on many other helicon plasma sources [23, 28, 29].

Figure 2(a) shows that the RF and ground connections of the birdcage are attached to diametrically-opposite points of one end-ring; the other end-ring is open at the point opposite the ground connection, giving the open coil equivalent electrical circuit in figure 2(b). The grounded extremities of the open coil are at the same potential and so can be connected together, as shown in figures 2(a) and (b), without affecting the electrical configuration of the open coil. In contrast, the simplest design of a birdcage is usually a closed coil, and the RF power is injected directly across one capacitor [12, 26]. However, a full analysis of the RF circuit [30] shows that a high input impedance is preferable to maintain the current amplitude uniformity and phase equality which are the desirable properties of normal modes; this is achieved here by widely separating the RF and ground connection positions.
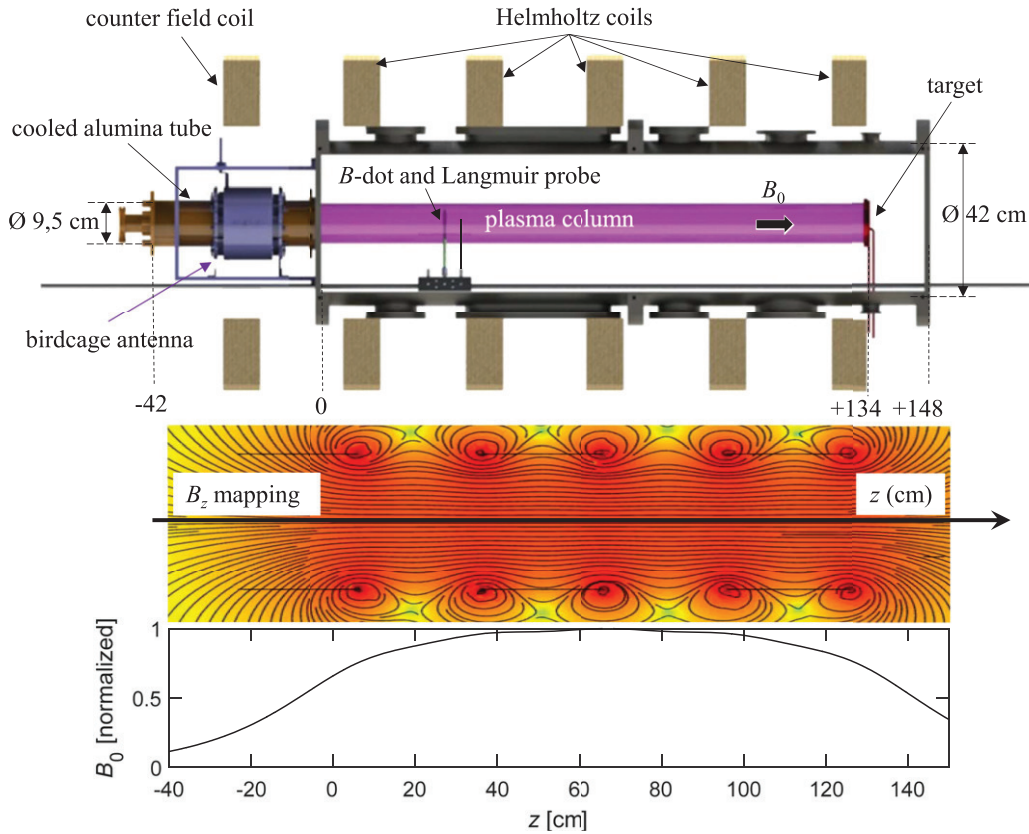
Figure 1. Top: experimental setup of RAID with its main elements, showing the *B*-dot and Langmuir axially-scanning probes. Centre: mapping of the static magnetic field amplitude (logarithmic colour scale) with magnetic field lines superposed. Bottom: axial profile of the normalized magnetic field of the Helmholtz coils.
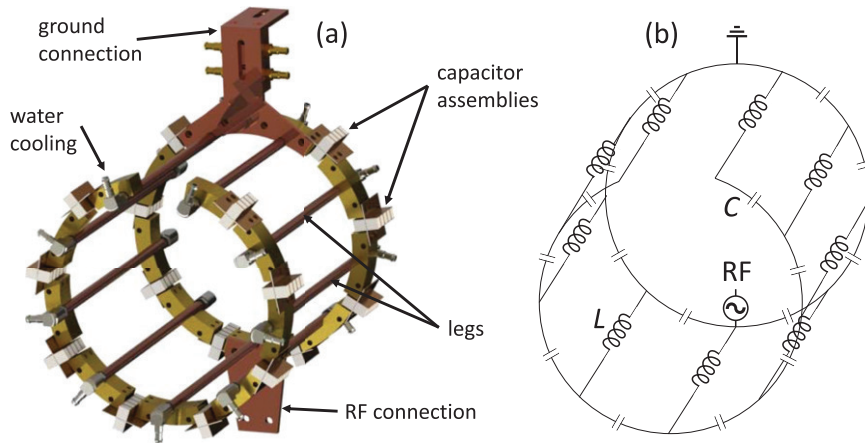

Figure 2. (a) Engineering drawing of the birdcage resonant antenna 13 cm diameter and 15 cm long, and (b) the equivalent electrical circuit.

$N - 1$ resonance modes can be excited in an open coil birdcage network with N legs [26, 30], but in an experiment such as RAID where the final goal is to obtain helicon regimes, an azimuthal cosine current distribution in the antenna legs is chosen. In the absence of plasma, this current distribution generates a uniform, transverse oscillating magnetic field over the birdcage cross-section, as commonly used in magnetic resonance imaging [26]. The birdcage antenna could therefore be expected to excite a linearly polarized wave, equivalent to the summation of right- and left-handed circular

polarizations, similar to the Nagoya III antenna [31–33]. However, it excites only the right handed mode, as commonly observed [2, 11, 31, 32, 34], because the left handed mode is strongly damped or only weakly excited [1, 11] in the plasma (see also section 4.3).

In practice, the capacitors' value, given the leg inductance, is selected so that the $\cos\theta$ first mode resonance [30] occurs at the 13.56 MHz frequency of the 15 kW RF power supply. To maximize the power transferred from the generator to the source, and to minimize ohmic losses in the
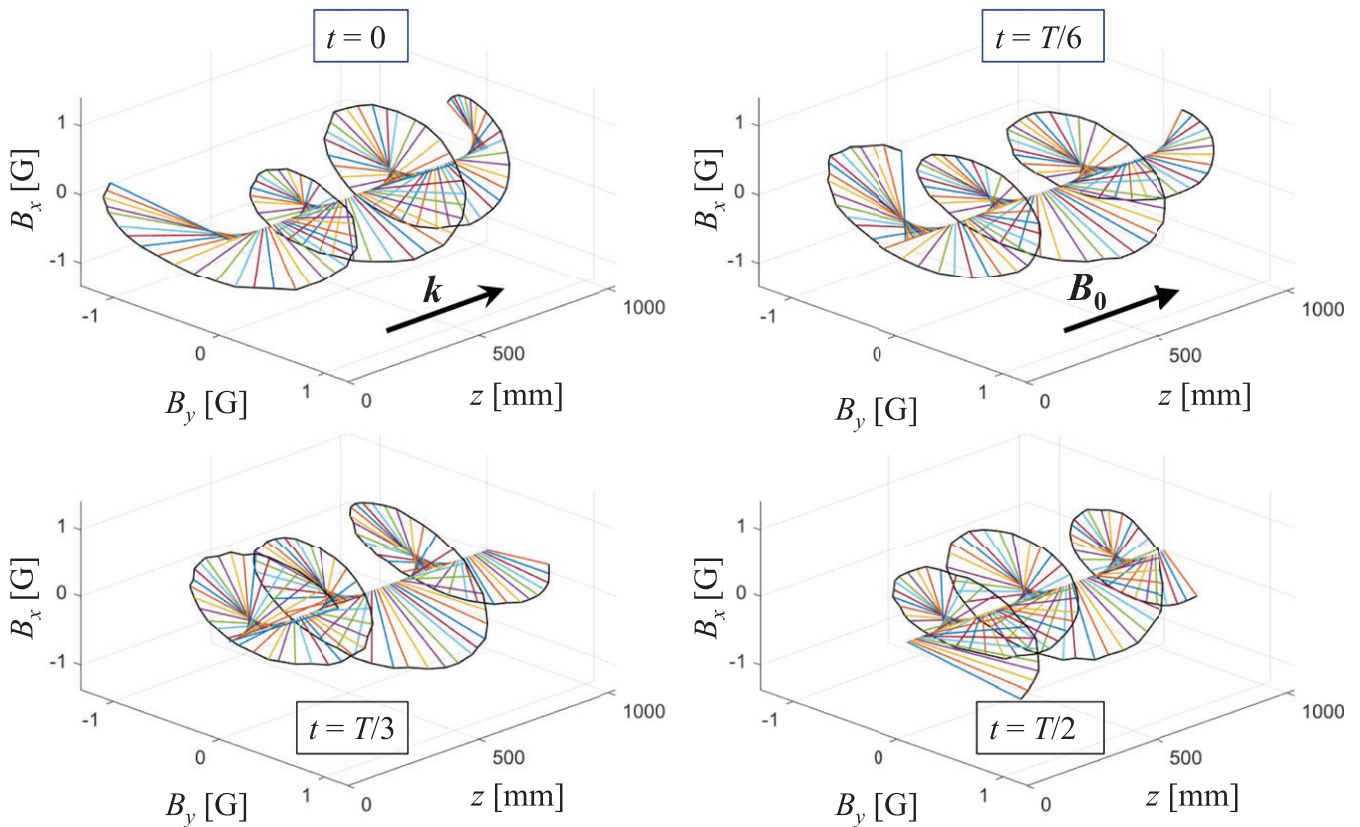
Figure 3. The transverse magnetic field raw data, measured on axis in Gauss, for three equal time intervals during an RF half-period ($t = 0, T/6, T/3, T/2$). The static magnetic field $\mathbf{B}_0$, and the wave vector $\mathbf{k}$ of propagation, are both oriented along the $+z$ axis as shown in the figure. Each chord is a perpendicular from the plasma column axis, at the z position where the measurement was made, to the $[B_x, B_y]$ value measured at that position. The helix is the locus of these $[B_x, B_y, z]$ points. The magnetic field spatial structure is seen to be a left-handed helix, rotating clockwise with respect to the direction of $\mathbf{B}_0$, in accordance with helicon theory. Hydrogen at 0.3 Pa, $B_0 = 200$ G, $P_{\mathrm{RF}} = 1.5$ kW.

transmission line, a matching box adapts the impedance between the generator's 50 Ω output impedance to an almost real antenna input impedance near resonance. The impedance of the antenna load varies with the plasma parameters, so feedback control of the matching vacuum capacitors was used to minimize reflected power.

The dominantly-real input impedance near to birdcage resonance [30] avoids the problem of strong reactive currents and voltages in the matching box and RF power connections of conventional helicon sources, because the high currents resonate only within the antenna itself. Conversely, conventional helicon sources are non-resonant, partial-helix antennas consisting of metal straps with very low impedance. A common antenna used for helicon sources is the half-right-turn helical antenna [32]. This antenna type was also tested on the RAID experiment, to compare with the resonant birdcage design. It was found that the resonant birdcage provides a wider range of operation parameters in terms of power (lower power modes) and higher pressure, with more stable discharges. In particular, helicon regimes can be difficult to ignite in hydrogen gas using conventional partial helix antennas, and if so, the discharges were very unstable [23, 35]. In contrast, the resonant antenna generates stable hydrogen discharges, which notably allowed the volumetric produc-

tion of hydrogen negative ions to be intensively studied on RAID [16–19].

The RAID axial static magnetic field was almost uniform [36, 37], with no magnetic mirrors or converging magnetic fields often used to aid light ion plasmas in other devices [21, 23, 29, 38–40]. Furthermore, the helicon mode was easily obtained and insensitive to the position of the gas flow input, with no apparent problems associated with pump-out [11] and neutral re-fuelling [24].

Principal electromagnetic wave frequencies are summarised in appendix A and table A1 for typical plasma parameters in RAID.

2.2. Probe diagnostics

Experimental measurements to demonstrate helicon wave propagation in RAID rely on two main diagnostics: a triple-axis B-dot probe, and a Langmuir probe. In order to have consistent measurements in the same plasma conditions, both probes were mounted on the same probe holder and moved with a scanning system along the axis of RAID (figure 1). The two probes were separated by 40 mm axially, and by 10 degrees in the cross-sectional plane to avoid shadowing.
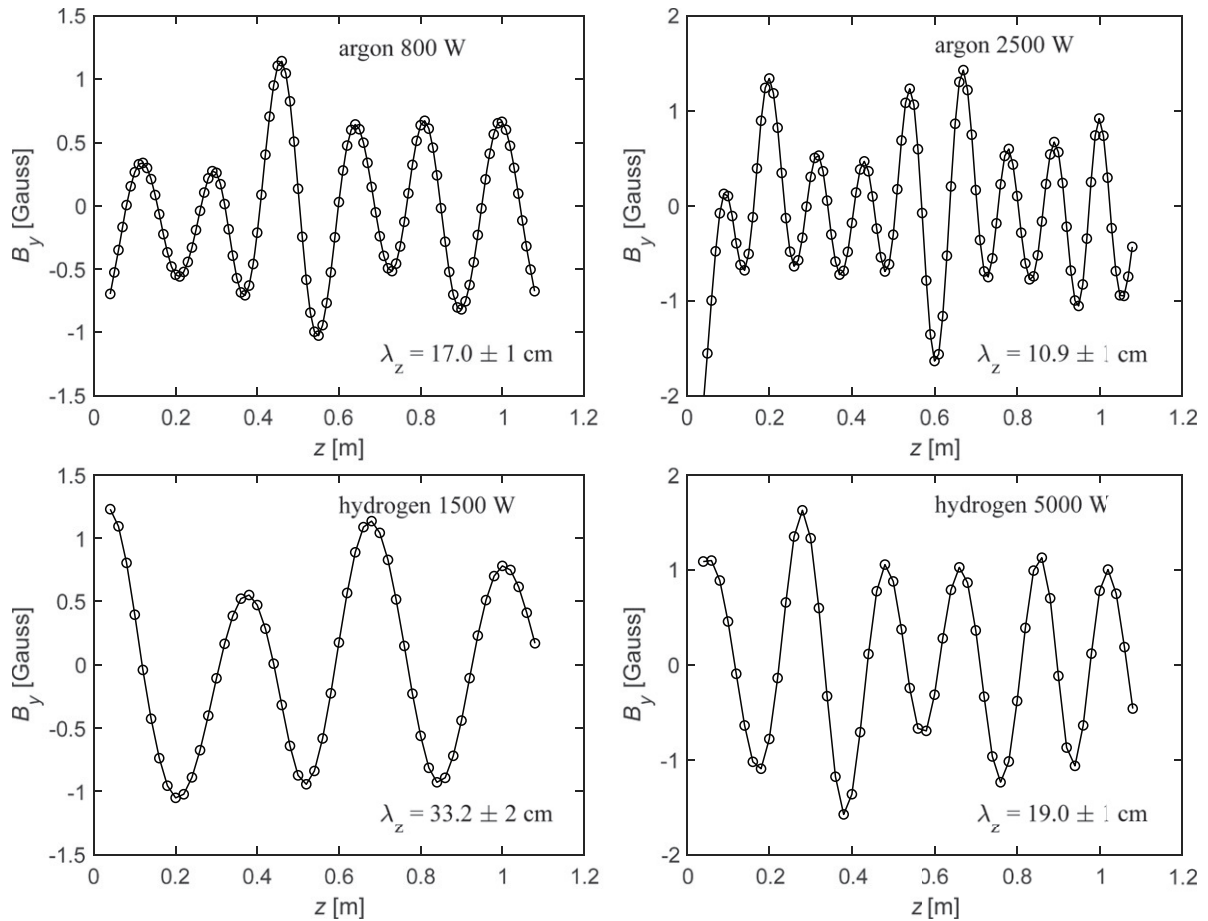
Figure 4. Examples of the B_y component of the measured field along the axis at a fixed temporal phase of an RF period, showing the measured wavelengths with their estimated variation along z. The upper graphs correspond to argon plasmas at two different RF powers; the lower graphs are for hydrogen plasmas. Pressure $= 0.3$ Pa, $B_0 = 200$ G, for both gases.

The Langmuir probe consists of an alumina stalk with a molybdenum tip 8 mm long and 0.4 mm diameter. The probe current/voltage characteristic was acquired for a voltage sweep from -40 to 10 V [16, 17].

The B-dot probe, described in more detail in reference [15], measures the oscillating B-field with three orthogonal coils mounted on an alumina probe head. The coils were wound with three turns of ceramic-insulated copper wire which can withstand temperatures up to 700 °C. The B-dot assembly was protected from the plasma heat load and ion bombardment inside an alumina cover. The connecting wires were twisted pairs to reduce magnetic pickup, passing through a stainless-steel tube as Faraday shield. After 1.5 m of shielded cable, each coil is connected to a hybrid combiner [41] which decouples the magnetic induction signal from the capacitive pickup. The three axes of the B-dot probe were calibrated in a known magnetic field at 13.56 MHz frequency in order to obtain absolute values [15]. The coil signal was triggered synchronously with a reference signal from the antenna current, and averaged over thousands of RF periods.

3. Experimental measurements of helicon waves

Figure 3 shows typical profiles of the transverse magnetic field measured along the axis z of the plasma column, where the static field $\mathbf{B}_0$ is oriented towards the target, in the same direction as the wave vector $\mathbf{k}$ (for H_2 at 0.3 Pa, $B_0 = 200$ G, $P_{RF} = 1.5$ kW). The field amplitude of ~ 1 G is typical of helicon waves and much smaller than the static field $\mathbf{B}_0$, so wave equations can justifiably be linearized [10]. The axial spatial structure of the transverse field is shown at four equally-spaced times in an RF half-period to show the rotation of the pattern. The wave has a left handed helical pitch which rotates clockwise in time. The wave therefore exhibits right handed polarization, defined as the direction of rotation of the local magnetic field about the steady axial magnetic field in the region near the axis of the plasma [2]. This confirms, at least qualitatively, the characteristics expected for a helicon wave field generated by the resonant birdcage antenna, as described in section 4.1. Quantitative agreement with the helicon dispersion relation is shown in section 4.4.
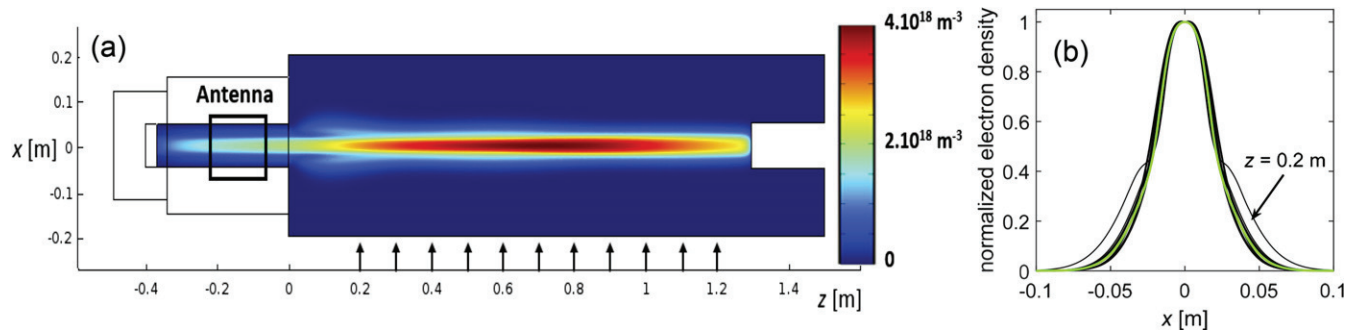
Figure 5. (a) Typical mapping of electron density measured in RAID in a (x, z) longitudinal plane for hydrogen plasma. (b) Black lines represent the normalized transverse profiles at the z positions indicated by arrows on (a); the green line is the mean profile used for integration of (6). The indicated profile at $z = 0.2$ m could be due to the radial discontinuity at the entrance of the vacuum chamber, or is possibly a spurious Langmuir probe signal caused by proximity to the antenna RF voltages.

Figure 4 shows measurements of the axial variation of one transverse component (B_y) of the magnetic field, at a given temporal phase, for different RF power and gas conditions. An axial wavelength λ_z is calculated from these measurements by taking the distance between consecutive extrema. This wavelength varies slightly (typically by a standard deviation of ± 1 cm about the mean value) along the plasma column, presumably because of the axial change of plasma density shown in figure 5. In fact, it can be seen in figure 4 that the wavelength in the $z = 0$–0.2 m region is always slightly longer than for the rest of the column, due to the fact that it is the lowest density region. These wavelength variations are nevertheless small enough so that a mean λ_z can be accurately estimated. The standing wave pattern of the field amplitude is characteristic of partial reflection of the wave occurring at the metal target of the chamber (figure 1), in presence of a small damping of the wave as expected for a low pressure regime (0.3 Pa) [4]. The wave is not totally reflected because the field amplitude envelope varies only by a factor ~ 2 along z in figure 4, probably because the target only presents a partial-area conducting boundary. We also note that the standing wave pattern was influenced by the electrical connection of the target (grounded or floating). Beating between different modes can be another cause of spatial modulation of the amplitude [29, 34], but in the presence of significant reflection, the latter is the more likely cause.

These axial wavelength measurements were performed for both argon and hydrogen discharges, varying either the RF power level P_{RF} or the static magnetic flux density $\mathbf{B}_0$ (for argon only). The characteristics of the plasma column, in terms of peak electron density, temperature and radial density profile, have been extensively studied and results are described notably in references [16, 17]. A typical mapping of the plasma density in a longitudinal plane is shown in figure 5(a), from measurements of the ion saturation current by scanning the plasma column with Langmuir probes [16, 17]. This was also used to map the electron temperature. Figure 5(b) shows 11 normalized transverse profiles taken at different z positions along the plasma column, which are indicated by arrows on figure 5(a). It can be seen that the radial profile of density varies only slightly in the major part of the beam. The green curve on figure 5(b) corresponds to the mean profile which was used as a

representative $n_e(r)/n_0$ function for the numerical integrations of (6), so only the peak electron density n_0 needed to be adjusted according to the RF power level or static magnetic flux density. The calibrated densities $n_0(P_{RF})$ and $n_0(B_0)$ were determined by 100 GHz interferometry absolute calibrated line-averaged densities, corrected for the density radial profile measured by the Langmuir probe, and the peak density was generally found to lie in the range 10^{18} to 10^{19} m^{-3} (figures 6 and 7). The estimated error bar in these densities was determined principally by the approximate $\pm 20\%$ error in the Langmuir probe measurements [16, 17]. For argon, the electron densities were high enough to use Thomson scattering [19], which confirmed the results obtained by interferometry, also shown on figure 6. The error bars for the Thomson scattering measurements were estimated from various sources of error such as the calibration of the polychromators [17, 19]. It can be seen from figure 7 that a change in magnetic flux density at fixed RF power also influences the peak electron density, reminding that B_0 and n_0 both define the axial wavelength of helicons (for a uniform plasma, $\lambda(z) \propto \sqrt{\frac{B_0}{n_0}}$ [42]). On the other hand, for the measurements performed at fixed magnetic field (200 G) in figure 6, the only variable is the density, and so we will mainly concentrate on these data for comparison with theory in section 4.

The plasma density in figures 6 and 7 varies smoothly with P_{RF} or B_0, whereas helicon discharges are sometimes characterized by stepped density evolutions [11, 42, 43]. This could be because the plasma column is not radially bounded in RAID, except for the antenna region, while for many helicon experiments the discharge is confined within a narrow dielectric tube of constant diameter [34]. Also, the partial reflection at the target could mean that a strict standing wave condition for total reflection is not imposed in RAID, permitting a continuous range of axial wavelengths.

Figure 8 shows the measured axial wavelengths λ_z, for both argon and hydrogen discharges, as a function of the plasma peak electron density according to figure 4, using the measured density relations $n_0(P_{RF})$ for both gases taken from figure 6. The evolution of the wavelength is smooth and continuous over the whole density range, although the plasma composition changes from heavy ions to light ions which could involve
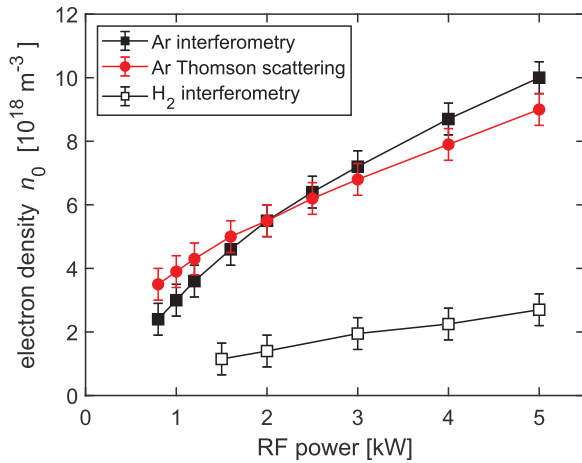
Figure 6. Peak electron density n_0 as a function of the input RF power (0.3 Pa, $B_0 = 200$ G) for argon and hydrogen discharges.
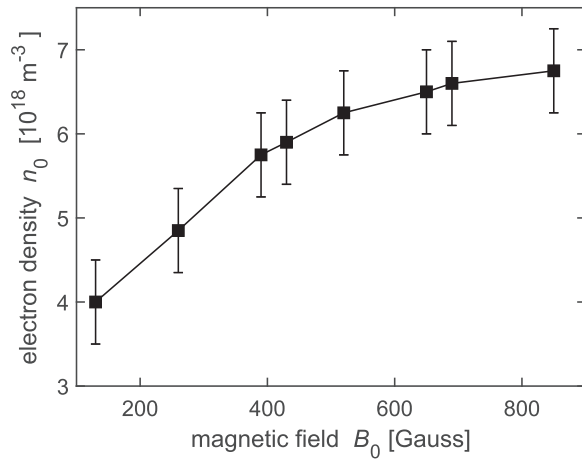

Figure 7. Peak electron density n_0 as a function of the static magnetic flux density B_0 (argon only, 0.3 Pa, $P_{RF} = 1500$ W).

different mechanisms of plasma heating. However, consideration of heating and absorption of Trivelpiece–Gould (TG) and helicon modes [11, 21, 23, 24, 29, 44, 45] is beyond the scope of this paper.

The change of gas type also implies a variation in the electron collision frequency, which then affects the damping of the wave. However, the collision frequency (typically $\nu = 1$–10 MHz) for the considered pressure (0.3 Pa) is expected to have only a very small influence on the propagation wavelength, which appears to be consistent with these measurements. This result also indicates that the wavelength is apparently not strongly affected by the small changes in the shape of the plasma column which occur when the RF power level or the gas type is changed. Furthermore, the smooth variation of λ_z shows that there is no preferred wavelength excited in relation to the antenna length (15 cm) [11]. Figure 8 summarizes the experimental measurements whose results are compared with theory in section 4.
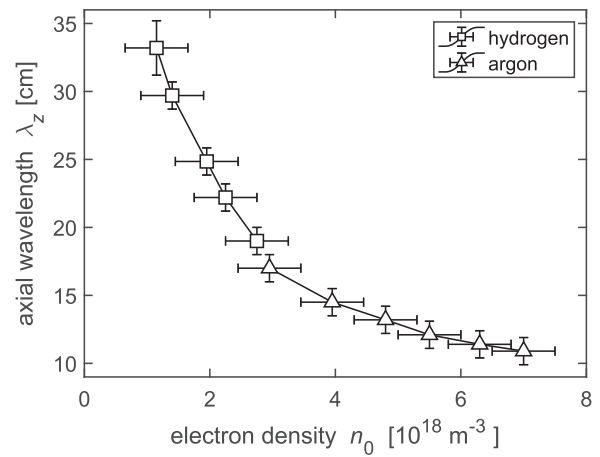

Figure 8. Measured axial wavelength λ_z (from figure 4) as a function of plasma peak density n_0 (from figure 6), at fixed magnetic field $B_0 = 200$ G. The error bars correspond to those in the respective figures 4 and 6. Squares correspond to hydrogen discharges, while triangles are for argon. These data are compared with theory in figure 13.

4. Comparison of helicon theoretical models with the experimental dispersion relation

Three theoretical models for helicon waves will be described, in order of increasing relevance for the experimental configuration. Two analytical models, for uniform plasma density (section 4.1), and radially non-uniform density (section 4.2), are followed by a numerical simulation in section 4.3. For each case, the theoretical results are compared with the experimental measurements in section 4.4.

4.1. Helicon mode theory: uniform plasma

We consider first order perturbations for the wave quantities, and neglect the ion contribution to the current density. For time harmonic variations ($e^{-i\omega t}$) of the perturbed quantities, the linearized first moment of Boltzmann's equation for the electron species provides an Ohm's law for the plasma medium, which can be expressed as [4]:

$$\mathbf{E} = \frac{1}{\epsilon_0 \omega_{pe}^2} \left[-i\hat{\omega}\mathbf{J} + \omega_{ce}\mathbf{J} \times \hat{\mathbf{e}}_z \right]. \tag{1}$$

In this expression $\mathbf{E}$ is the perturbed electric field, $\mathbf{J}$ is the associated current density, and $\hat{\mathbf{e}}_z$ is the unit vector along z. $\omega_{ce} = \frac{qB_0}{m_e}$ is the electron cyclotron frequency, with q the magnitude of the elementary charge and m_e the electron mass; $\hat{\omega} = \omega + i\nu$, where ω is the angular RF frequency, ν is the electron effective momentum transfer frequency due to collisions with neutrals, and $\omega_{pe} = \sqrt{\frac{q^2 n_e}{\epsilon_0 m_e}}$ is the electron plasma frequency. The equation set is completed by Maxwell's equations:

$$\nabla \times \mathbf{E} = i\omega\mathbf{B}, \tag{2}$$

$$\nabla \times \mathbf{B} = \mu_0\mathbf{J} - i\frac{\omega}{c^2}\mathbf{E}, \tag{3}$$

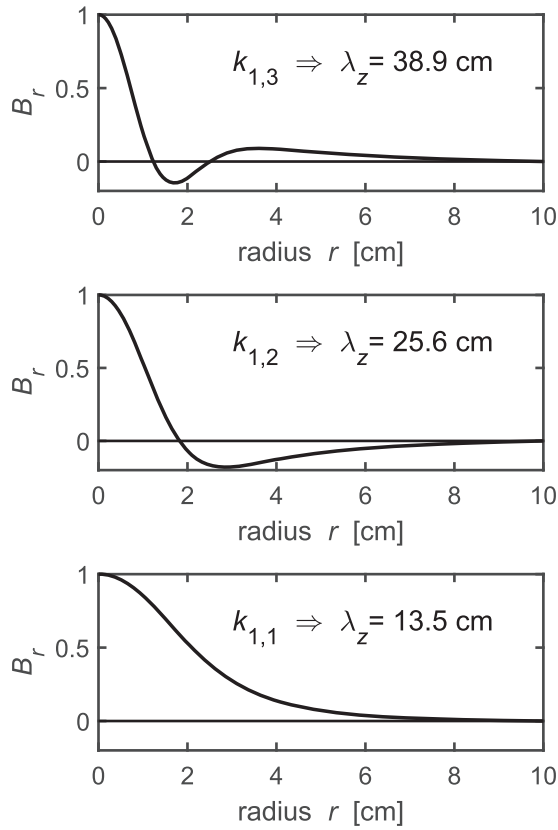where $\mathbf{B}$ is the perturbed magnetic flux density.

Figure 9. The first three eigenfunctions of the B_r radial profile calculated for the $n_e(r)$ radial profile of figure 5 with $n_0 = 5 \times 10^{18}$ m^{-3}, $B_0 = 200$ G, and $m = 1$.
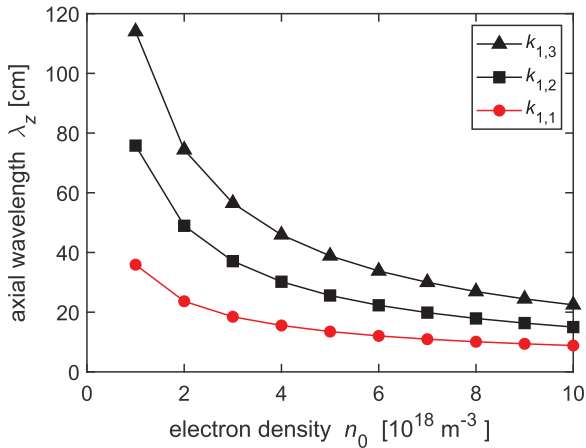

Figure 10. Evolution of the axial wavelengths λ_z, corresponding to the $k_{1,n}$ eigenvalues ($n = 1, 2, 3$), as a function of the peak electron density n_0, for the radial profile $n_e(r)$ of figure 5. The wavelengths for the $k_{-1,n}$ eigenvalues are much longer (not shown) and show no match to experiment. The red curve is compared with experiment in figure 13.

Assuming infinite, uniform plasma density, the plane wave whistler dispersion relation can be determined analytically from these three equations. The principal electromagnetic electron R wave propagating along $\mathbf{B}_0$ [7, 42, 46] is

given by:

$$\frac{k^2}{k_0^2} = 1 - \frac{\omega_{pe}^2}{\omega(\omega - \omega_{ce})}, \tag{4}$$

where $k_0 = \omega/c$, and k is the z component of the wave vector in this work. The polarization is right handed circular, with left handed helical pitch, as observed in the experimental measurements of figure 3.

In the present case of $\omega \ll \omega_{ce} < \omega_{pe}$, (4) simplifies to the well-known helicon wave dependence on electron density and magnetic flux density for propagation along $\mathbf{B}_0$ [7, 42],

$$k^2 = n_e q \omega \mu_0 / B_0. \tag{5}$$

The relation between plane wave solutions and cylindrical eigenmodes is explained by Boswell [47] and Davies [48]. Using axial wavelength $\lambda_z = 2\pi/k$, (5) gives a good fit to the experimental measurements in figures 13 and 14, provided that a mean density $\bar{n}_e = 0.5 n_0$ is used as a fitting parameter [2, 11].

4.2. Helicon mode theory: non-uniform plasma

The analysis of helicon wave propagation conventionally considers a longitudinally infinite, axisymmetric plasma column, magnetized by a uniform and static magnetic field $\mathbf{B}_0$ aligned with the column axis, which is generally set to coincide with the z axis of a cylindrical coordinate system (r, θ, z). Longitudinal and azimuthal invariance imply an $e^{i(m\theta + kz)}$ variation of perturbed quantities, with m the azimuthal mode number and $k = \frac{2\pi}{\lambda_z}$ the longitudinal component of the wave vector. The full solution (but still neglecting the displacement current) of the constant density cylindrical model [49] shows that the dispersion relation is given by the superposition of two branches distinguished by their different radial wavelengths. The helicon branch is characterized by a long radial wavelength, typically comparable to the plasma radius, and is almost undamped. The second one, the so-called TG branch, exhibits much smaller radial wavelengths which are highly damped. This latter branch is dominantly excited on the edge of the plasma column and is thought to play an important role for the energy deposition process into the discharge. Besides this last aspect, for sufficiently high magnetic field B_0, the TG branch is so rapidly damped, inwards from the plasma edge, that the overall radial profile of the total wave field is almost identical to the helicon branch alone.

In terms of quantitative diagnostic analysis, the main parameter we can access experimentally is the axial wavelength λ_z in figures 4 and 8, and consequently the required theoretical background essentially concerns the dispersion relation for helicons.

As already mentioned, an analytical expression can be established for constant density profiles, but this approach nevertheless presents two major drawbacks for our data analysis. First, the hypothesis of a constant density profile is far from the experimental situation in figure 5. Second, the dispersion relation obtained implies a coupling between longitudinal and transverse helicon and TG wave numbers, so that to compare the experimental data with the theoretical predictions,
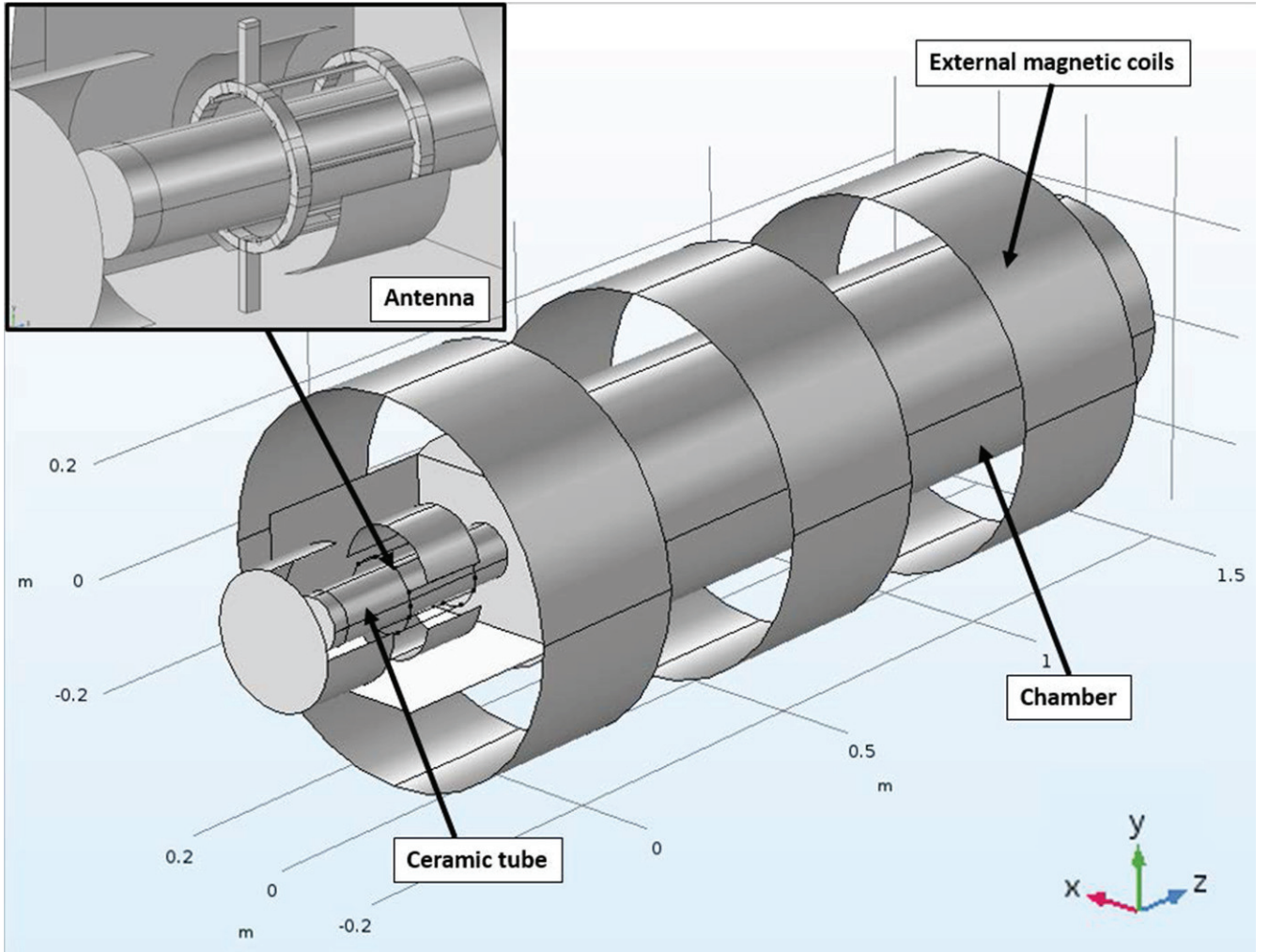
Figure 11. Numerical representation of the RAID experiment. The six coils in figure 1 coincide with the edges of the external magnetic coils in this figure. The inset shows the birdcage resonant antenna surrounded by two half-cylinder screens.

both longitudinal and transverse wavelengths would have to be measured. The transverse wavelengths are typically expected to lie in a range of 10^{-3} to 10^{-2} m (depending on the TG or helicon branch respectively) for our experimental conditions, and our B-dot probe system does not have a sufficient spatial resolution and radial positioning precision for such small wavelengths to be measured correctly.

Therefore, we use another approach which can be applied to radially non-uniform plasma provided that the 'helicon approximation' is valid [34, 50, 51] whereby the $-i\hat{\omega}\mathbf{J}$ term in (1) is neglected (see appendix B). By doing so, the TG branch is removed from the solution and only the helicon branch remains. The helicon approximation allows a second order differential equation to be established for the radial component B_{r} of the magnetic field:

$$B_{\mathrm{r}}'' + f(r)B_{\mathrm{r}}' + g(r)B_{\mathrm{r}} = 0, \quad \text{where:} \tag{6}$$

$$f(r) = \frac{k_{\mathrm{p}}^2 r^2 - 3m^2}{r(k_{\mathrm{p}}^2 r^2 - m^2)},$$

$$g(r) = \frac{1 - m^2}{r^2} + k_{\mathrm{p}}^2 \left[1 - \frac{2}{k_{\mathrm{p}}^2 r^2 - m^2}\right]$$

$$- k_{\mathrm{p}}^2 \psi^2 n_{\mathrm{e}}^2(r) - \frac{2mk_{\mathrm{p}}^2 \psi}{k_{\mathrm{p}}^2 r^2 - m^2} n_{\mathrm{e}}(r)$$

$$+ \frac{m\psi}{r} n_{\mathrm{e}}'(r),$$

and $\quad k_0 = \dfrac{\omega}{c}, \quad k_{\mathrm{p}}^2 = k_0^2 - k^2, \quad \psi = \dfrac{q^2 k_0^2}{k_{\mathrm{p}}^2 \omega \omega_{\mathrm{ce}} \epsilon_0 m_{\mathrm{e}}}.$

Equation (6) can be integrated numerically for a given plasma density profile $n_{\mathrm{e}}(r)$, the coefficients $f(r)$ and $g(r)$ being non-singular for all r. Attention has nevertheless to be paid to the boundary conditions, as detailed in appendix B. At $r = 0$, arguments of symmetry and of non-diverging quantities provide the initial conditions for the numerical integration. The vacuum chamber wall at $r = a$ is a perfectly conducting outer boundary where the radial component of the current density must vanish, $J_{\mathrm{r}}(a) = 0$, or equivalently $B_{\mathrm{r}}(a) = 0$ (appendix B). For a given $n_{\mathrm{e}}(r)$ profile, magnetic field B_0 and mode number m, the vanishing radial current condition can only be fulfiled for discrete values of k, which are the system's eigenvalues defined as $k_{m,n}$, where m refers to the azimuthal mode number and n designates the eigenvalue number ($n = 1$ corre-
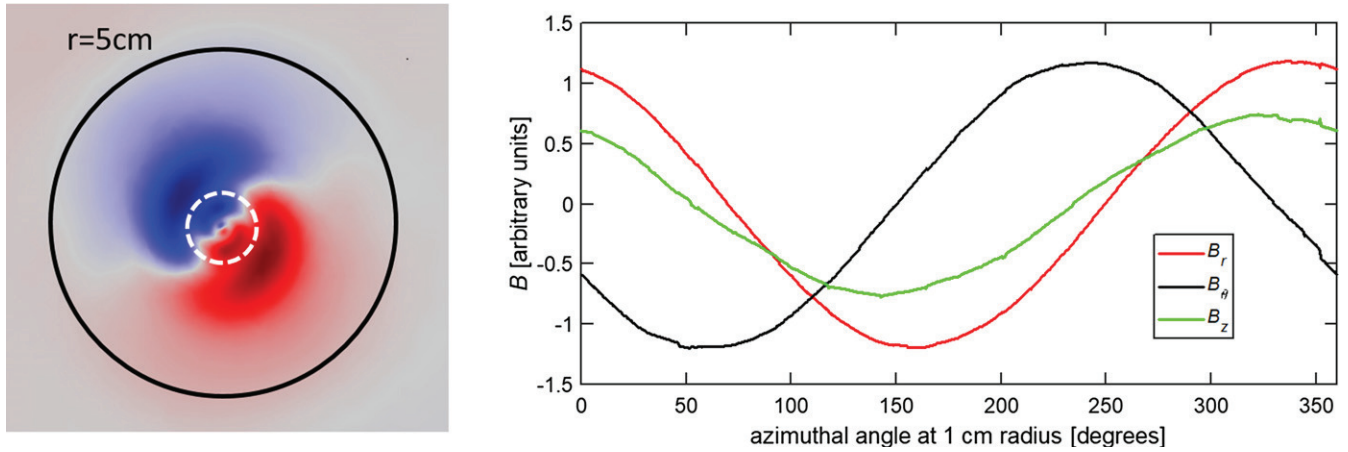
Figure 12. Left: azimuthal cross-section of the B_z wave field component, calculated by the numerical simulation at $z = 75$ cm according to figure 5. Right: B_r, B_θ, and B_z components calculated around the circumference of the white dashed circle at 1 cm radius, showing a dominant $m = 1$ symmetry. The black circle marks the approximate plasma radius of 5 cm. The magnetic fields are in arbitrary units.
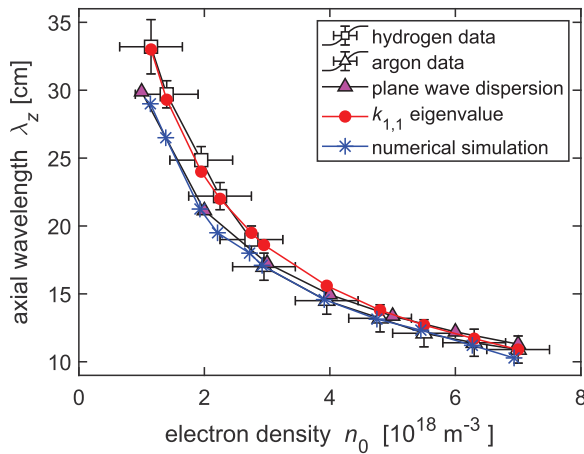

Figure 13. Variation of the axial wavelength λ_z as a function of the peak electron density n_0 for $B_0 = 200$ G, showing a comparison between experimental data, analytical, and numerical results. The open symbols (partly obscured) represent the measured axial wavelengths taken from figure 8. The magenta triangles indicate the plane wave dispersion relation from section 4.1 for an assumed average density $\bar{n}_e = 0.5 n_0$. The full red circles correspond to the $k_{1,1}$ eigenvalue in figure 10 arising from the integration of (6) in section 4.2. The blue stars show the results of the COMSOL [54] numerical simulation in section 4.3.

sponding to the shortest value of λ_z). As an illustration, figure 9 shows the first three eigenfunctions obtained by numerically integrating (6) for the $n_e(r)$ profile of figure 5 and for $m = 1$ (for an arbitrary peak density). These radial variations of a few cm are too short to be spatially resolved by the B-dot probe. In contrast, the dependence of the $k_{1,n}$ eigenvalues with the peak electron density shown on figure 10 ($\lambda_z = \frac{2\pi}{k_{1,n}}$) encompass a range of axial wavelengths which can be easily measured by the B-dot probe. In particular, the $k_{1,1}$ curve, shown in red, provides a very good fit to the experimental data [11] in figure 13 as discussed in section 4.4. Complementary and alternative methods include references [52, 53] and citations of these works.

4.3. Numerical simulation

In addition to the above theoretical approach, a 3D finite elements model (COMSOL [54] electromagnetic module) of the RAID experiment was developed to calculate the wave propagation generated by the birdcage antenna (figure 11). To match the model to the experimental conditions as closely as possible, the magnetic field of the external coils around the RAID chamber was computed, as shown in the lower part of figure 1. This field is almost uniform, so no matrix transformation was necessary for the simulation to follow strongly non-uniform magnetic field contours as in devices with magnetic mirror configurations [23]. For the wave calculations, the magnetized plasma was considered to be an axisymmetric cold-plasma-dielectric medium, of conductivity given by (1), so that only Maxwell's equations (2) and (3) are to be solved numerically. The imposed plasma density mapping [23] is taken from figure 5 with the peak electron densities n_0 of figure 6 or 7. To estimate the local electron-neutral effective collision frequency ν, the Bolsig+ software [55] for both argon and hydrogen was used to obtain the T_e dependence of the collision rate, assuming Maxwellian electron energy distributions. Finally, the antenna structure (figure 2) is excited by the RF input voltage, and all the resultant antenna currents and wave fields are calculated self-consistently.

Instead of assuming an $m = +1$ wave field symmetry [23], the full wave simulation was carried out with no imposed symmetry. The numerical solution spontaneously converged to the wavelength λ_z and azimuthal symmetry of the $k_{+1,1}$ eigenvalue of figure 10, as shown by the close fit of the numerical simulation data to the theoretical and experimental curves in figure 13. The calculated magnetic wave field components in figure 12 also show a dominant $m = 1$ symmetry. Therefore the experimentally-observed $m = +1$ mode dominance [1, 2, 11, 31, 32, 34] is apparently an implicit property of Maxwell's equations in this configuration, without invoking any thermal or kinetic effects, nor constraints of minimum energy or entropy.
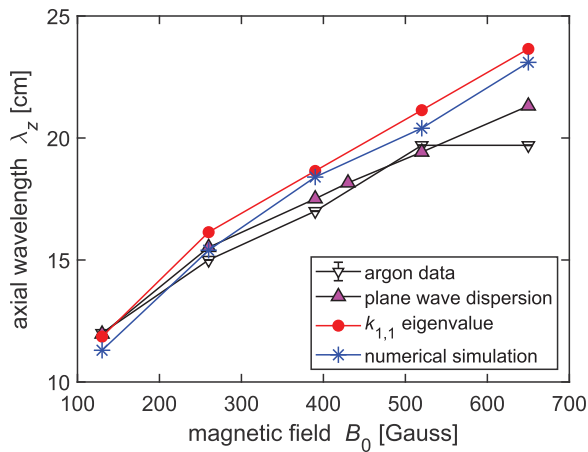
Figure 14. Variation of the axial wavelength λ_z as a function of the magnetic flux density B_0, accounting for the plasma density variation using figure 7, showing a comparison between experimental, theoretical, and numerical results. The symbols are described in the caption of figure 13.

4.4. Comparison with the experimental data

The experimental measurements of the axial wavelength of figure 8 are reproduced in figure 13 for comparison with the three models as follows:

From section 4.1, the right hand polarized plane wave dispersion relation for propagation along $\mathbf{B}_0$ in uniform plasma density [1, 2, 7, 29, 42, 46] shows good agreement using a fitted parameter for the mean density $\bar{n}_e = 0.5n_0$ [2, 11].

From section 4.2, the $k_{1,1}$ curve given by the non-uniform density theoretical model shows good agreement with no fitted parameters, indicating that the $m = 1$ mode is the dominantly excited mode, as reported in many other works [2, 31, 32, 34], and with the shortest possible value for the axial wavelength λ_z, i.e. $n = 1$ [11].

From section 4.3, the numerical simulation spontaneously reproduces the experimental measurements and the form of the $k_{1,1}$ mode.

Finally, we show on figure 14 the evolution of the helicon wavelength measured in argon discharges for various values of the DC magnetic flux density B_0 at fixed RF power level. Here again, the $k_{1,1}$ eigenvalue provides a reasonably good fit to the experimental data, as confirmed also by the results of the numerical simulation.

To summarize, the axial wavelength is apparently not determined by the antenna length [11], nor by standing waves in the cavity, but varies smoothly, depending on the plasma density and the magnetic field, satisfying the dispersion relation of the helicon wave [56] excited by the birdcage antenna. The helicon is an electron mode, whose dispersion relation depends on the plasma (electron) density and magnetic field intensity, but not on the ion mass. Hence the independence of the axial wavelength with respect to the gas type in figure 8 (and figure 13) is consistent with helicon theory.

5. Conclusions

A resonant birdcage antenna was shown to be a suitable source for helicon plasmas, generating an intense, stable plasma column in argon or hydrogen up to 10 kW of continuous RF power.

The magnetic wave field measured along the plasma axis exhibited the helical structure and polarization consistent with helicon waves. The dependence of axial wavelength on the plasma density and external DC magnetic field was smooth and continuous, showing no preferred dependence on the antenna length, nor the standing wave structure. Furthermore, heavy or light ions (Ar^+ or H_2^+) had no notable influence on the axial wavelength, which depended only on the electron density and the DC magnetic field as expected according to helicon theory.

Finally, the measured axial wavelengths were compared with semi-analytical and purely numerical models. The semi-analytical model relies on the so-called 'helicon approximation' to calculate the eigenvalues for any radially non-uniform plasma profile, by numerical integration of a second order differential equation. The experimental data and the calculated $m = 1$ eigenvalue of lowest axial wavelength are in good agreement with no fitted parameters. Numerical simulation of the self-consistent currents in the antenna and the plasma spontaneously converged towards this same dominant mode.

In conclusion, the birdcage helicon source presents a new alternative to conventional partial-helix antennas, with technical advantages regarding high internal resonance currents and predominantly-real input impedance, and a wider operational parameter space with improved plasma stability, especially for light ion (hydrogen) plasmas.

Acknowledgments

Data availability statement

The data that support the findings of this study are available upon reasonable request from the authors.

Appendix A. Typical wave frequencies

In order to situate the plasma conditions and frequencies with respect to parameters commonly used in the literature, table A1 shows typical values for H_2 and Ar plasma at $B_0 = 200$ G

Table A1. Approximate expressions for the cutoff and resonance angular frequencies ω (rad s^{-1}) of the principal electromagnetic plane waves (collisionless, cold uniform plasma, but including mobile ions) [42]. The plasma angular frequency is $\omega_p = (\omega_{pe}^2 + \omega_{pi}^2)^{1/2}$. ω_{UH} and ω_{LH} are the upper and lower hybrid angular frequencies, respectively. Example frequencies f (Hz) are given for H$_2^+$ and Ar$^+$ at $B_0 = 200$ G and $n_0 = 10^{18}$ m^{-3} for comparison with the RF frequency 13.56 MHz.

Wave	ω cutoff	f cutoff	ω resonance	f resonance
R	$\approx \frac{\omega_{ce} + \sqrt{\omega_{ce}^2 + 4\omega_p^2}}{2}$	9.27 GHz	ω_{ce}	560 MHz
L	$\approx \frac{-\omega_{ce} + \sqrt{\omega_{ce}^2 + 4\omega_p^2}}{2}$	8.71 GHz	ω_{ci}	H$_2$: 153, Ar: 7.63 kHz
		9.27 GHz	$\omega_{UH}^2 \approx \omega_p^2 + \omega_{ce}^2$	9.00 GHz
X	Both as above	8.71 GHz	$\frac{1}{\omega_{LH}^2} \approx \frac{1}{\omega_{pi}^2} + \frac{1}{\omega_{ce}\omega_{ci}}$	H$_2$: 9.23, Ar: 2.06 MHz
O	ω_p	8.98 GHz	—	—

and $n_0 = 10^{18}$ m^{-3}. The frequency ordering is $\omega_{ci} \ll \omega_{rf} \ll \omega_{ce} \ll \omega_p$, which is characteristic of whistler and helicon waves [7, 42, 46], so ion and displacement currents can be neglected [1, 4, 29]. The RF frequency 13.56 MHz is relatively close to the lower hybrid frequency ω_{LH} in H$_2$ [57], but quite different from that in Ar where coupling is more efficient, suggesting that the lower hybrid frequency is not a special frequency for power transfer in RAID. Also, the lower hybrid frequency is less than the RF frequency for both the Ar and H$_2$ ions, which is not indicative of different heating regimes for heavy and light ions in terms of fast and slow wave penetration [21].

Appendix B. The helicon approximation, and derivation of a second order differential equation for B_r in a radial profile of electron density

The purpose of this appendix is to guide the reader through the derivation of the second order differential equation for the radial component B_r of the helicon wave, which can be numerically integrated for any radial profile of plasma density $n_e(r)$. This equation is obtained in the framework of the 'helicon approximation', and original papers by F F Chen *et al* can be found in references [34, 50, 51].

The 'helicon approximation' consists in neglecting the $-i\hat{\omega}\mathbf{J}$ term in (1), which holds provided that $\frac{\hat{\omega}}{\omega_{ce}} \ll 1$ and that all the components of $\mathbf{J}$ are of comparable amplitude. The measurements shown in figure 8 were performed with $B_0 = 200$ G and 13.56 MHz RF frequency, for which $\frac{\omega}{\omega_{ce}} \sim 0.02$, so the helicon approximation can be applied. The impact of collisions is also removed from the problem by this approximation, but it can be shown, in the framework of the constant density model, that collisions are expected to have very little impact on the axial wavelength of helicons in the considered pressure range ($\sim$0.1–1 Pa). Then (1) can be written as

$$\mathbf{E} = \frac{\omega_{ce}}{\epsilon_0 \omega_{pe}^2}\mathbf{J} \times \hat{\mathbf{e}}_z = \alpha\mathbf{J} \times \hat{\mathbf{e}}_z, \tag{B.1}$$

where the function $\alpha(r) = \frac{\omega_{ce}}{\epsilon_0\omega_{pe}^2}$ is a function of radius because the radially non-uniform density, $n_e(r)$, means that the electron plasma frequency is also a function of radius, $\omega_{pe}(r)$.

The equation set is completed by Maxwell's equations (2) and (3). Taking the curl of (B.1) and using (2) we get the relation:

$$\nabla \times \mathbf{E} = \nabla \times [\alpha\mathbf{J} \times \hat{\mathbf{e}}_z] = \alpha\nabla \times [\mathbf{J} \times \hat{\mathbf{e}}_z]$$
$$+ \alpha'\hat{\mathbf{e}}_r \times \mathbf{J} \times \hat{\mathbf{e}}_z = i\omega\mathbf{B},$$
$$\Rightarrow \alpha\nabla \times [\mathbf{J} \times \hat{\mathbf{e}}_z] - \alpha'J_r\hat{\mathbf{e}}_z = i\omega\mathbf{B}, \tag{B.2}$$
$$\text{where} \quad \alpha' = \partial_r\alpha.$$

Because we are looking for modes of cylindrical symmetry, we state an $e^{i(m\theta + kz - \omega t)}$ dependence for first order perturbations. Under this ansatz, it can then be easily shown that $\nabla \times [\mathbf{J} \times \hat{\mathbf{e}}_z] = ik\mathbf{J} - (\nabla \cdot \mathbf{J})\hat{\mathbf{e}}_z$, and (B.2) becomes:

$$i\omega\mathbf{B} = ik\alpha\mathbf{J} - \alpha(\nabla \cdot \mathbf{J})\hat{\mathbf{e}}_z - \alpha'J_r\hat{\mathbf{e}}_z. \tag{B.3}$$

Note that taking the cross product of (B.3) with $\hat{\mathbf{e}}_z$ we get the relation:

$$\omega\mathbf{B} \times \hat{\mathbf{e}}_z = k\alpha\mathbf{J} \times \hat{\mathbf{e}}_z \Leftrightarrow J_\perp = \frac{\omega}{k\alpha}B_\perp. \tag{B.4}$$

Combining the curl equation for $\mathbf{B}$ in (3), the helicon approximation (B.1), and (B.4), we obtain:

$$\nabla \times \mathbf{B} = \mu_0\mathbf{J} - i\frac{\omega}{c^2}\mathbf{E} = \mu_0\mathbf{J} - i\frac{\omega\alpha}{c^2}\mathbf{J} \times \hat{\mathbf{e}}_z = \mu_0\mathbf{J} - \frac{ik_0^2}{k}\mathbf{B} \times \hat{\mathbf{e}}_z, \tag{B.5}$$

where $k_0 = \frac{\omega}{c}$. Taking once again the cross product of (B.5) with $\hat{\mathbf{e}}_z$, and re-using (B.4), we finally obtain:

$$\left[\nabla \times \mathbf{B} + \frac{ik_0^2}{k}\mathbf{B} \times \hat{\mathbf{e}}_z - \frac{\mu_0\omega}{k\alpha}\mathbf{B}\right] \times \hat{\mathbf{e}}_z = 0. \tag{B.6}$$

With $\mathbf{B} = \begin{pmatrix} B_r(r) \\ B_\theta(r) \\ B_z(r) \end{pmatrix} e^{i(m\theta + kz - \omega t)}$, (B.6) provides the coupled equations:

$$-kB_z' + ik_p^2B_r - k_0^2\frac{\omega_{pe}^2}{\omega\omega_{ce}}B_\theta = 0 \tag{B.7}$$

$$-\frac{ikm}{r}B_z - ik_p^2B_\theta + k_0^2\frac{\omega_{pe}^2}{\omega\omega_{ce}}B_r = 0, \tag{B.8}$$

where $k_p^2 = k_0^2 - k^2$ is the transverse wave number in vacuum. The system of simultaneous equations is completed by $\nabla \cdot B = 0$, which is written as

$$\frac{1}{r}B_r + B_r' + \frac{im}{r}B_\theta + ikB_z = 0. \tag{B.9}$$

Eliminating B_θ and B_z using (B.8) and (B.9), the remaining equation (B.7) yields the second order non-linear differential equation for B_r given in (6) of section 4.2, as required.

This equation has the great advantage of presenting no problematic singularity, as $(k_p^2 r^2 - m^2)$ never vanishes (because k_p is generally complex and even purely imaginary in the limit $k \gg k_0$). Numerical integration is straightforward starting from $r = 0$, but some attention has to be paid to the initial conditions. The leading idea is that we want non-diverging quantities at the origin.

It must be noted that the functions $f(r)$ and $g(r)$ in (6) come from the division of the originally-obtained second order differential equation by the coefficient of B_r'', which in fact vanishes at $r = 0$ so that this normalization is not valid at the origin. At $r = 0$, the original equation is:

$$(1 - m^2)B_r(0) = 0. \tag{B.10}$$

This relation generally implies $B_r(0) = 0$, apart for the values $m = \pm 1$ which are special because they are the only ones for which the B_r component of the field does not have to vanish at the origin.

We now consider symmetry arguments. To do so we momentarily switch to a Cartesian coordinate system with the unit vector $\hat{e}_x$ aligned with the $\theta = 0$ direction. We have:

$$B_x(x) = -B_r(r)\cos(m\pi) \quad \text{for } x < 0$$

$$\Rightarrow B_x(-x) = -B_x(x) \quad \text{for even values of } m,$$

$$B_x(x) = B_r(r) \quad \text{for } x > 0$$

$$\Rightarrow B_x(-x) = B_x(x) \quad \text{for odd values of } m.$$

$$\tag{B.11}$$

$B_x(x)$ is then an even function of x for odd values of m, which implies that the derivative $\partial_x B_x$ must vanish at $x = 0$ (provided that we search for smooth functions at the origin, i.e. no discontinuity of the first derivative). Conversely, for even values of m, $\partial_x B_x$ generally does not vanish at the origin (although it can).

We then finally have:

(a) For odd values of $m \neq \pm 1$: $B_r(0) = 0$ and $\partial_r B_r(0) = 0$.
(b) For $m = \pm 1$: $B_r(0) = 1$ (normalization) and $\partial_r B_r(0) = 0$.
(c) For even values of m: $B_r(0) = 0$ and $\partial_r B_r(0) = 1$ (normalization).

Eigenvalues k are determined by a boundary condition at the plasma edge, usually a vanishing radial magnetic field, $B_r(a) = 0$ (B.4).

ORCID iDs

A A Howling ⓘ https://orcid.org/0000-0003-4417-4339
I Furno ⓘ https://orcid.org/0000-0001-8348-1716

References

[1] Klozenberg J P, McNamara B and Thonemann P C 1965 *J. Fluid Mech.* **21** 545
[2] Lehane J A and Thonemann P C 1965 *Proc. Phys. Soc.* **85** 301
[3] Boswell R W 1975 *Nature* **258** 58
[4] Chen F F 1991 *Plasma Phys. Control. Fusion* **33** 339
[5] Boswell R W and Chen F F 1997 *IEEE Trans. Plasma Sci.* **25** 1229
[6] Chen F F 2015 *Plasma Sources Sci. Technol.* **24** 014001
[7] Chen F F 2016 *Introduction to Plasma Physics and Controlled Fusion* 3rd edn (Heidelberg: Springer)
[8] Stenzel R L 2019 *Phys. Plasmas* **26** 080501
[9] Boswell R W 1970 A study of waves in gaseous plasmas *PhD Thesis* School of Physical Sciences, Flinders University of South Australia
[10] Boswell R W 1970 *Phys. Lett.* A **33** 457
[11] Boswell R W 1984 *Plasma Phys. Control. Fusion* **26** 1147
[12] Guittienne P, Chevalier E and Hollenstein C 2005 *J. Appl. Phys.* **98** 083304
[13] Furno I, Agnello R, Fantz U, Howling A, Jacquier R, Marini C, Plyushchev G, Guittienne P and Simonin A 2017 *EPJ Web Conf.* **157** 03014
[14] Marini C *et al* 2017 *Nucl. Fusion* **57** 036024
[15] Jacquier R *et al* 2019 *Fusion Eng. Des.* **146** 1140
[16] Agnello R *et al* 2020 *Nucl. Fusion* **60** 026007
[17] Agnello R 2020 Negative hydrogen ions in a helicon plasma source *PhD Thesis* EPFL Lausanne, Switzerland no. 7817 https://doi.org/10.5075/epfl-thesis-7817
[18] Agnello R *et al* 2018 *Rev. Sci. Instrum.* **89** 103504
[19] Agnello R, Andrebe Y, Arnichand H, Blanchard P, De Kerchove T, Furno I, Howling A A, Jacquier R and Sublet A 2020 *J. Plasma Phys.* **86** 905860306
[20] Lumsdaine A *et al* 2020 *Fusion Eng. Des.* **160** 112001
[21] Goulding R H *et al* 2017 *Fusion Sci. Technol.* **72** 588
[22] Rapp J *et al* (The MPEX team) 2017 *Nucl. Fusion* **57** 116001
[23] Piotrowicz P A, Caneses J F, Green D L, Goulding R H, Lau C, Caughman J B O, Rapp J and Ruzic D N 2018 *Plasma Sources Sci. Technol.* **27** 055016
[24] Piotrowicz P A, Caneses J F, Showers M A, Green D L, Goulding R H, Caughman J B O, Biewer T M, Rapp J and Ruzic D N 2018 *Phys. Plasmas* **25** 052101
[25] Karpman V I, Kaufman R N and Shagalov A G 1984 *J. Plasma Phys.* **31** 209
[26] Jin J-M 1998 *Electromagnetic Analysis and Design in Magnetic Resonance Imaging* (Boca Raton, FL: CRC Press)
[27] Howling A A, Guittienne P, Jacquier R and Furno I 2015 *Plasma Sources Sci. Technol.* **24** 065014
[28] Shoji T, Sakawa Y, Nakazawa S, Kadota K and Sato T 1993 *Plasma Sources Sci. Technol.* **2** 5
[29] Caneses J F and Blackwell B D 2016 *Plasma Sources Sci. Technol.* **25** 055027
[30] Guittienne P, Howling A A and Hollenstein C 2014 *Plasma Sources Sci. Technol.* **23** 015006
[31] Light M and Chen F F 1995 *Phys. Plasmas* **2** 1084
[32] Sudit I D and Chen F F 1996 *Plasma Sources Sci. Technol.* **5** 43
[33] Okamura S *et al* 1986 *Nucl. Fusion* **26** 1491
[34] Light M, Sudit I D, Chen F F and Arnush D 1995 *Phys. Plasmas* **2** 4094

[35] Sakawa Y, Takino T and Shoji T 1999 *Phys. Plasmas* **6** 4759
[36] Thompson D S, Agnello R, Furno I, Howling A, Jacquier R, Plyushchev G and Scime E E 2017 *Phys. Plasmas* **24** 063517
[37] Thakur S C *et al* 2020 arXiv:2005.11214v2
[38] Carter M D *et al* 2002 *Phys. Plasmas* **9** 5097
[39] Mori Y, Nakashima H, Baity F W, Goulding R H, Carter M D and Sparks D O 2004 *Plasma Sources Sci. Technol.* **13** 424
[40] Yoshitaka M, Hideki N, Baity F W Jr, Goulding R H, Carter M D and Sparks D O 2006 *Thin Solid Films* **506–507** 583
[41] Borg G G and Jahreis T 1994 *Rev. Sci. Instrum.* **65** 449
[42] Lieberman M A and Lichtenberg A J 2005 *Principles of Plasma Discharges and Materials Processing* 2nd edn (New York: Wiley)
[43] Perry A J, Vender D and Boswell R W 1991 *J. Vac. Sci. Technol.* B **9** 310
[44] Borg G G and Boswell R W 1998 *Phys. Plasmas* **5** 564
[45] Degeling A W, Borg G G and Boswell R W 2004 *Phys. Plasmas* **11** 2144
[46] Swanson D G 2003 *Plasma Waves* 2nd edn (*Series in Plasma Physics*) (Bristol: Institute of Physics Publishing)
[47] Boswell R W 1984 *J. Plasma Phys.* **31** 197
[48] Davies B 1970 *J. Plasma Phys.* **4** 43
[49] Chen F F and Arnush D 1997 *Phys. Plasmas* **4** 3411
[50] Chen F F, Hsieh M J and Light M 1994 *Plasma Sources Sci. Technol.* **3** 49
[51] Sudit I D and Chen F F 1994 *Plasma Sources Sci. Technol.* **3** 602
[52] Krämer M 1999 *Phys. Plasmas* **6** 1052
[53] Breizman B N and Arefiev A V 2000 *Phys. Rev. Lett.* **84** 3863
[54] COMSOL Inc 2021 *Multiphysics software from COMSOL* http://comsol.com
[55] Hagelaar G J M and Pitchford L C 2005 *Plasma Sources Sci. Technol.* **14** 722
[56] Komori A, Shoji T, Miyamoto K, Kawai J and Kawai Y 1991 *Phys. Fluids* B **3** 893
[57] Zhu P and Boswell R W 1989 *Phys. Rev. Lett.* **63** 2805